

communications physics

ARTICLE



<https://doi.org/10.1038/s42005-022-00903-5>

OPEN

Soliton linear-wave scattering in a Kerr microresonator

Pierce C. Qureshi^{1,2}, Vincent Ng^{1,2}, Farhan Azeem^{1,3}, Luke S. Trainor¹, Harald G. L. Schwefel^{1,3}, Stéphane Coen^{1,2}, Miro Erkintalo^{1,2} & Stuart G. Murdoch^{1,2}✉

The nonlinear scattering of a linear optical wave from a conservative soliton has been widely studied in optical fibers as a mechanism for nonlinear frequency conversion. Here we extend this analysis to consider the scattering of an externally injected probe wave from a dissipative cavity soliton circulating in a Kerr microresonator. We demonstrate, both theoretically and experimentally, that this nonlinear interaction can be harnessed for useful expansion of the soliton frequency comb via the formation of a secondary idler comb. We explore the physics of the process, showing that the phase detuning of the injected probe from a cavity resonance plays a key role in setting the central frequency of the idler comb, thus providing a convenient parameter through which to control the spectral envelope of that comb. Our results elucidate the dynamics that govern the interactions between dissipative Kerr cavity solitons and externally injected probe waves, and could prove useful in the design of future Kerr frequency comb systems by enabling the possibility to provide high-power comb lines in a specified spectral region simply through the injection of a suitably chosen probe.

¹Department of Physics, University of Auckland, Auckland 1010, New Zealand. ²The Dodd-Walls Centre for Photonic and Quantum Technologies, Dunedin, New Zealand. ³Department of Physics, University of Otago, Dunedin 3016, New Zealand. ✉email: s.murdoch@auckland.ac.nz

Microresonator frequency combs (microcombs) offer an attractive pathway towards the realization of miniaturized, low-power coherent optical frequency combs^{1–3}. Applications of these chip-scale devices have already been demonstrated across fields ranging from telecommunications⁴ and spectroscopy⁵ to remote sensing^{6,7} and medical diagnostics⁸. In the vast majority of systems, the resonators are driven with a monochromatic laser, and frequency combs form through the third-order optical Kerr nonlinearity¹. In such systems, coherent comb states are underpinned by the excitation of ultra-short localized structures known as temporal cavity solitons⁹ – also referred to as dissipative Kerr solitons^{2,10}.

The spectral properties of Kerr microcombs are dominantly set by the material and geometric parameters of the microresonator. A key comb property is its spectral bandwidth, which (to leading-order) scales as¹¹

$$\Delta f \propto \sqrt{\frac{\gamma P_{\text{in}} \mathcal{F}}{|\beta_2|}}, \quad (1)$$

where γ , \mathcal{F} , and β_2 are the resonator's Kerr nonlinearity coefficient, finesse, and group-velocity dispersion (GVD) at the driving wavelength, and P_{in} is the driving power, respectively. The large \mathcal{F} and γ of microresonators are thus highly conducive to the realization of combs with large spectral bandwidth. In addition, the dispersion of microresonators can be engineered to provide further increase in the attainable comb bandwidth. This typically involves both lowering the resonator's GVD coefficient $|\beta_2|$, and optimizing its third-order dispersion so as to allow additional spectral extension through the formation of dispersive waves that are phase-matched to the pump^{12–14}.

Very recently, a new approach has been put forward that allows for the spectral characteristics and extent of microcombs to be controlled even after the fabrication of the resonator (whereupon its material and geometric properties are set). Specifically, the injection of a frequency-shifted probe field alongside the main comb generating pump has been shown to permit controllable expansion of the comb spectrum via two distinct mechanisms^{15–17}. In the first mechanism^{15,16}, a cavity soliton excited by the pump field imparts a nonlinear phase shift on the intracavity field of the frequency-shifted probe. This induces a frequency comb structure around the probe frequency via cross-phase modulation (XPM). In the second mechanism, frequency components of the soliton comb are spectrally translated through the four-wave-mixing process of nonlinear Bragg scattering¹⁷, again giving rise to a comb structure around the frequency-shifted probe field. Both mechanisms result in the generation of a secondary comb around the probe frequency, with line spacing equal to the spacing of the original soliton comb, yet they rely on fundamentally different physical phenomena: incoherent XPM^{15,16} and coherent Bragg scattering¹⁷.

Recent experiments have unequivocally demonstrated the application potential of Bragg-scattering spectral expansion: a coherent Kerr microcomb with an expanded bandwidth of 1.6 octaves was reported in¹⁷. However, a number of questions remain open with regards to the physics that underpin the phenomenon. For instance, earlier studies^{18,19} have shown that nonlinear Bragg scattering of a frequency comb can be understood as the frequency-domain description of a particular soliton-linear wave interaction^{20–23} that has been extensively studied in the context of conservative (single-pass) nonlinear fibre optics^{24–27}. This raises the question as to whether the simple phase-matching conditions known to govern the process in the single-pass case hold predictive power in the resonator context. In addition, nonlinear Bragg scattering is intrinsically a coherent FWM (four-wave mixing) process, and could therefore be envisaged to depend upon the linear detuning of the probe wave from

a cavity resonance; however, no discussion of the role of detuning has hitherto been presented.

Here we theoretically and experimentally study the spectral extension of soliton microcombs via coherent FWM Bragg-scattering. We show that the simple phase-matching condition that underpins soliton-linear wave interactions in single-pass systems¹⁹ remains valid in the resonator context, provided however that the phase detuning of the probe wave is appropriately accounted for. Indeed, we find that this detuning plays a key role in the process, providing a convenient parameter through which to control the spectral characteristics of the comb extension. We perform experiments in a magnesium-fluoride (MgF_2) micro-disk resonator, and demonstrate the generation of frequency tunable, low-noise idler combs that possess identical line spacing, and the same low-noise characteristics, as the driving cavity soliton comb. We further highlight the flexibility of this comb expansion technique by swapping the spectral locations of the cavity soliton pump and the probe wave whilst still maintaining the required phasematching – and hence comb extension. Our results provide significant insights into the spectral extension of soliton microcombs, and highlight the intimate linkage between Bragg scattering spectral extension and soliton-linear wave interactions that have been studied widely in the context of nonlinear fiber optics and supercontinuum generation^{18–27}. Whilst our experimental results are obtained in a monolithic crystalline microresonator we expect these results to find useful application across all microresonator platforms.

Results

Soliton linear-wave scattering. We begin by briefly recounting how interactions between solitons and weak linear waves can enact resonant energy transfer to new frequencies in Kerr media^{20–23,28–31}. Considering a superposition field $E = S + p$, where S and p represent the soliton and the probe, respectively, the Kerr nonlinearity $|E|^2 E$ will after linearization with respect to p yield three terms: $|S|^2 S$, $2|S|^2 p$, and $S^2 p^*$. Each of these three terms can drive resonant energy transfer to new waves³⁰, provided that those waves are phase-matched to one of the driving terms. In fact, the first term is responsible for the generation of the standard dispersive waves that are directly phasematched with the soliton^{28,29}. On the other hand, the second and third terms represent nonlinear mixing between the soliton and the weak probe wave, and can drive additional phasematched radiation processes^{20–23,31}. In particular, the $2|S|^2 p$ interaction has been shown to drive both the incoherent XPM and coherent FWM Bragg scattering interactions²².

Earlier studies have shown that the soliton-linear wave interaction can be understood in the frequency domain as a cascade of individual FWM Bragg scattering processes^{18,19}. Specifically, pairs of discrete frequency components of a periodic train of solitons can act as pumps that drive a Bragg scattering cascade that translates the incident linear wave to a new idler frequency [see Fig. 1(a), (b)]. Remarkably, this cascade can be phase-matched even though none of the elementary FWM processes are phase-matched^{18,19,32}; moreover, the phase-matching condition of the entire cascade is (approximately) the same as that of the soliton-linear wave interaction driven by the nonlinear polarization term $2|S|^2 p$. In what follows, we show that this result extends to resonator configurations by demonstrating that the spectral extension of soliton microcombs via FWM Bragg scattering obeys the phasematching condition of the pertinent time-domain soliton-linear wave interaction.

Soliton linear-wave phasematching. To derive the soliton-linear wave phasematching condition in a resonator configuration, we

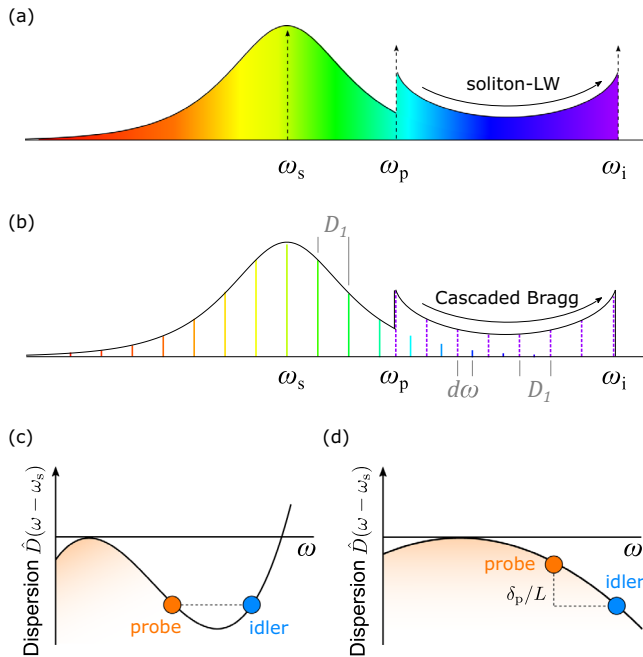


Fig. 1 Soliton-linear wave scattering. **a** Schematic illustration of the interaction between a soliton at ω_s and a weak linear wave (LW) at ω_p . The interaction enables the flow of energy to a phase-matched idler wave at ω_i . **b** Frequency domain description of the soliton-linear wave interaction in **a**, showing how the energy flow can be described as a cascade of nonlinear Bragg-scattering events. Components of the newly-generated idler comb are all shown in purple for clarity. The idler comb possesses the same free spectral range $= D_1/(2\pi)$ but is offset from the soliton comb (by $d\omega$). **c**, **d** visualize the phasematching of the process in single-pass and resonator configurations, respectively. **c** In single-pass configurations, higher-order dispersion is required for phasematching. **d** The extra degree of freedom provided by the probe detuning δ_p relaxes the phasematching condition in resonators.

note that the phase accumulated by the linear idler wave at frequency ω_i over one round trip is: $\phi_i = \beta(\omega_i)L - \omega_i t_R$, where $\beta(\omega)$, L , and t_R are respectively the propagation constant, length, and round trip time of the resonator. Phase-matching is achieved when $\phi_i = \phi_p + 2\pi m$, where $\phi_p = -\omega_p t_R$ is the phase accumulated by the externally-injected probe wave (at the input to the resonator) and m is an integer³³. Expanding the propagation constant $\beta(\omega)$ as a Taylor-series around the soliton pump, ω_s , we obtain

$$\hat{D}(\omega_i - \omega_s)L = \delta_p + \hat{D}(\omega_p - \omega_s)L + 2\pi q, \quad (2)$$

where δ_p is the phase detuning of the injected probe from the cavity resonance closest to it, and the reduced dispersion

$$\hat{D}(\omega - \omega_s) = \beta(\omega) - \beta(\omega_s) - \frac{t_R}{L}(\omega - \omega_s) \quad (3)$$

$$= \sum_{k \geq 2} \frac{\beta_k}{k!} (\omega - \omega_s)^k. \quad (4)$$

The coefficient $q = m - m_0$ with m_0 the mode index of the resonance closest to ω_p describes phase-matching to higher-order resonant sidebands that will not be considered in this work; in what follows, we set $q = 0$. We note that the analysis presented above considers only linear contributions to the idler's phase-matched frequency. Cross phase modulation between the idler wave and the other intracavity fields present will contribute an additional nonlinear contribution to this shift^{14,34}. The magnitude of this nonlinear shift can be estimated by comparing the

difference between the idler frequency shift obtained from a generalized Lugiato-Lefever equation (LLE) simulation that includes all nonlinear contributions (see Methods) and that predicted by Eq. (2). For the experimental parameters used in this work, we find the difference between these two values to be only of the order of a few percent. For this reason we omit these terms from our phasematching analysis.

Equation (2) is akin to the phasematching condition for Bragg-type soliton-linear wave interactions in single-pass fibre configurations¹⁹, but with the additional probe detuning δ_p accounting for the resonant nature of the system. Importantly, the presence of δ_p significantly relaxes the phasematching requirements: whilst higher-order dispersion is required in single-pass configurations, in resonators phasematching can be achieved even with a purely quadratic dispersion profile [see Fig. 1(c), (d)]. Explicitly, for a resonator with second-order dispersion only, the (angular) frequency detuning $\Omega_i = \omega_i - \omega_s$ of the newly generated idler field from the soliton pump satisfies:

$$\Omega_i^2 = \Omega_p^2 + \frac{2\delta_p}{\beta_2 L}, \quad (5)$$

where $\Omega_p = \omega_p - \omega_s$. It is worth noting that Eq. (5) predicts two phasematched idler frequencies symmetrically located either side of the cavity soliton pump. However, the FWM Bragg cascade to the idler frequency located on the opposite side of the cavity soliton to the probe will require a cascade with substantially more steps and hence be less efficient. Indeed, for the parameters used in this paper, only the idler frequency closest to the probe frequency is observed in simulations and experiments. For different resonator parameters, however, it may be possible to efficiently drive both cascades resulting in new spectral components generated on both sides of the cavity soliton¹⁷.

Illustrative simulations. To confirm the analysis above, we performed numerical simulations using the generalized LLE (see Methods), and compared the simulations to predictions based on Eq. (5). Figure 2 shows results from simulations that use parameters similar to the experiments that will follow (see figure caption). In particular, the false colour plot in Fig. 2(a) shows the spectral envelope of the intracavity field as a function of the probe phase detuning δ_p normalized to the resonance half-width ($\Delta_p = \delta_p/\alpha$), where α corresponds to half the intracavity power lost per roundtrip. To obtain this plot, at each probe detuning a cavity soliton is first excited (at $\Omega = \omega - \omega_s = 0$) and allowed to stabilize before the probe field is turned on. Also, in Fig. 2(c)–(f) we show lineplots of selected spectra in more detail, whilst Fig. 2(g)–(j) show the corresponding temporal intensity profile of the intracavity field over a single roundtrip.

In addition to the broadband soliton field around $\Omega = 0$ and the injected probe field at Ω_p , a third wave whose position changes continuously with the probe detuning is clearly visible. This corresponds to the idler comb that is generated via the soliton-linear wave interaction described above. Indeed, in Fig. 2(b) we plot the peak frequency shift of the idler comb as a function of the probe detuning, superimposed with the theoretical prediction of the phasematched frequency given by Eq. (5). The agreement between the simulated idler frequency and the theoretical prediction is very good, validating the use of the linearised phasematching expression of Eq. (5) for our experimental parameters. When the probe detuning is sufficiently close to its own resonance [with $\Delta_p \in (-3, 11)$], our simulations predict that the soliton-linear wave interaction is interrupted. This occurs because the probe itself undergoes modulation instability within this range of detunings, as clearly evidenced by the characteristic modulation instability spectral features

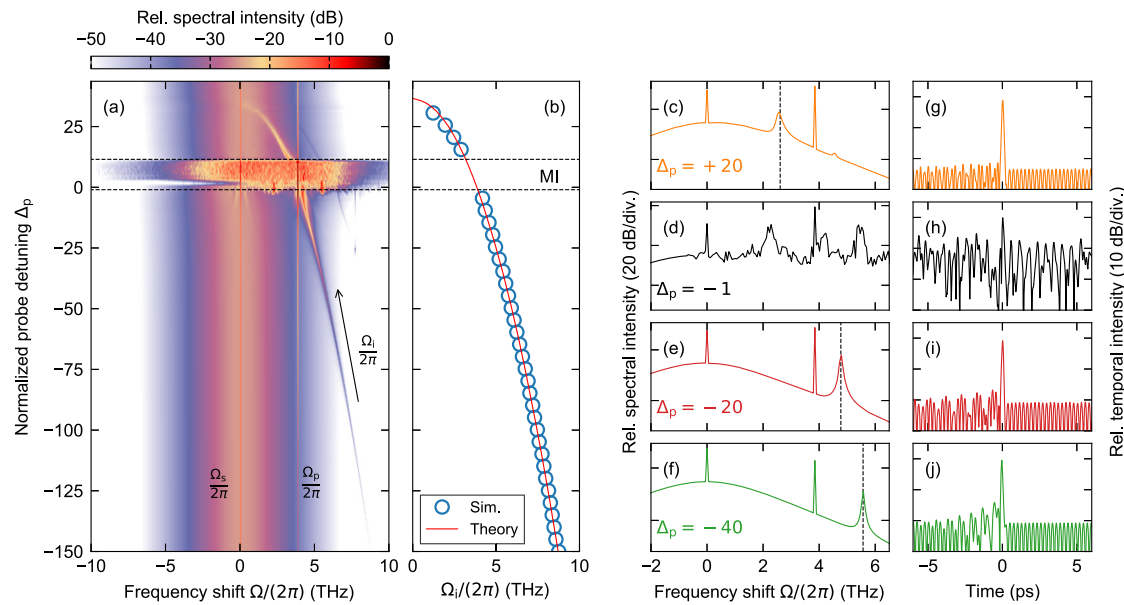


Fig. 2 Numerical simulation of soliton-linear wave interactions in a Kerr microresonator. **a** Pseudo-color plot shows the intracavity spectrum as a function of the probe detuning normalized to half the cavity linewidth, $\Delta_p = \delta_p/\alpha$. The x-axis denotes the frequency offset from the soliton-generating pump, $\Omega = \omega - \omega_s$. Ω_s , Ω_p , and Ω_i respectively denote angular frequency detunings of the soliton ($\Omega_s = 0$), the probe, and the idler. **b** Circles show the peak frequency detuning of the idler comb as a function of the linear probe detuning Δ_p as extracted from the simulation data in **(a)**. Solid red curve in **(b)** shows the phasematched frequency predicted by Eq. (5). Dashed horizontal lines in **(a)**, **(b)** delineate the region within which the probe undergoes modulational instability and prohibits the soliton-linear wave interaction. **c-f** show individual spectra from **(a)** at selected probe detunings as indicated, with dashed vertical lines indicating the phasematched idler frequencies predicted by Eq. (5). **g-j** show the temporal intensity of the intracavity fields corresponding to the spectra shown in **(c-f)**. The simulation results were obtained using the Lugiato-Lefever equation as described in Methods, with parameters similar to the experiments that will follow: $\mathcal{F} = 3.1 \times 10^4$, $\gamma = 1.4 \times 10^{-3} W^{-1} m^{-1}$, $\beta_2 = -3.2 \times 10^{-27} s^2 m^{-1}$, $P_{in,i} = |E_{in,i}|^2 = 80$ mW, with $i = (s, p)$, and $\theta = 1 \times 10^{-4}$.

observed in Fig. 2(a). For most detunings within this range, the large intensity fluctuations of modulation instability prevent the persistence of the cavity soliton altogether^{39,40} and accordingly prohibit any soliton-linear wave interaction. However, for a narrow sliver of detunings [with $\Delta_p \in (-3, 1)$], our simulations predict that the cavity soliton can coexist with the modulation instability state associated with the probe, and in this case a linear wave interaction can take place, but with the noise from the probe's modulation instability transferred to both the soliton and the idler combs, resulting in low-coherent states. This noise-like modulation instability structure can be clearly seen in the spectral and temporal traces obtained at $\Delta_p = -1$ plotted in Fig. 2(d), (h). The incoherence arising from modulation instability is in stark contrast with the results seen at the other detunings shown in Fig. 2(c, g), (e, i) and (f, j). Here, simulations confirm that both the soliton and idler combs are coherent as required for useful spectral extension, and stable temporal structures are observed with the newly generated idler wave manifesting itself in the time domain as an oscillatory tail on the soliton's leading edge. At this point, we note that the simulations presented here consider equal driving powers for the soliton and external probe fields. Simulations and theoretical considerations show that the efficiency of the soliton-linear wave cascade is set by the soliton pump power only¹⁸. Varying the external probe power will thus result in the power in the idler comb simply scaling proportionally. The exact value of probe power used does, however, play an important role in the range of probe detunings Δ_p over which modulation instability is observed in the probe field, with larger probe powers resulting in wider regions of modulation instability.

Experiments. For experimental demonstration, we use a setup that is built around an MgF₂ micro-disk with a free spectral range

(FSR) of 58.4 GHz (see Methods)^{41–43}. The micro-disk is driven by three continuous-wave lasers: A C-band pump laser at 1550 nm, an L-band pump laser 1582 nm, and a third laser at 1534 nm configured to act as an auxiliary pump that provides thermal compensation during the cavity soliton excitation^{44,45}. The two pump lasers are coupled to the same mode family, and they can interchangeably act as the soliton-generating pump and the probe field. The auxiliary laser (wavelength fixed at 1534 nm) is coupled to a different mode-family of the resonator to ensure it does not participate in the soliton-linear wave dynamics.

We first set the wavelength of the L-band pump to 1582 nm and excite a cavity soliton at that wavelength. The remaining C-band laser acts the probe, and is tuned into resonance close to 1550 nm from the blue-detuned (negative Δ_p) side. Figure 3(a)–(c) show the comb spectra measured at the output of the resonator as the probe detuning is scanned into resonance. We can clearly observe an idler peak that moves towards the probe as the detuning Δ_p is increased. The idler peak tunes continuously until we reach the modulation instability region of the probe field, at which point the cavity soliton ceases to exist and the soliton-linear wave interaction is halted – in accordance with our simulations [see Fig. 2(a), (b)]. We then reset the experiment such that a new cavity soliton is excited at 1582 nm, and tune the probe field into resonance from the red-detuned (positive Δ_p) side. Figure 3(d)–(f) show the resulting spectra, and we again observe the appearance of an idler peak that continuously tunes towards the probe, now as Δ_p is decreased. These results are in qualitative agreement with the phasematching prediction of Eq. (5), with positive (and negative) probe detunings observed to generate idler peaks at frequencies that are below (and above) the original probe frequency.

Figure 3 (g)–(l) show the low-frequency RF (radio frequency) spectra of each microcomb state shown in Fig. 3(a)–(f). All of the

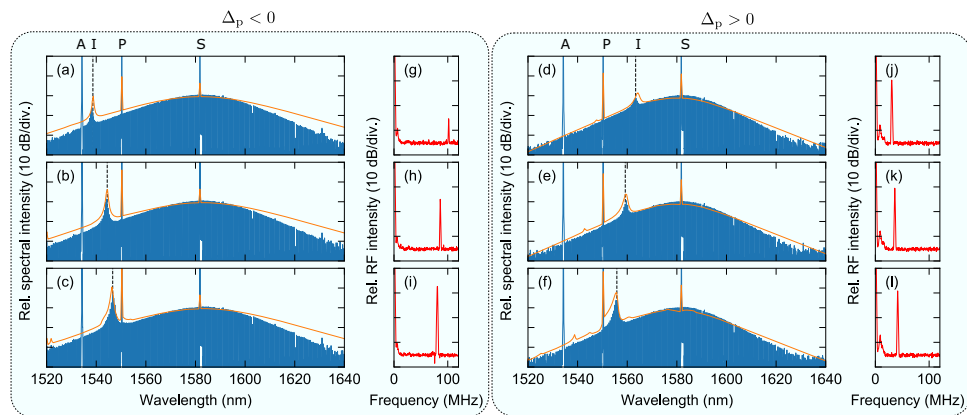


Fig. 3 Experimental spectra with the soliton-generating pump at 1582 nm and the probe at 1550 nm. **a–c** Blue curves show microcomb spectra measured at the resonator output for different negative values of the probe detuning, such that the idler is generated at wavelengths shorter than the probe. Orange curves show corresponding results from simulations and the dashed vertical lines show the phasematched wavelength predicted by Eq. (5). **d–f** show spectra as in **(a–c)** but for different positive values of the probe detuning, such that the idler is generated at wavelengths longer than the probe. **g–l** Radio-frequency (RF) spectra corresponding to **(a–f)**. The beat frequencies in the RF spectra correspond to the offset between the soliton and the idler combs, $d\omega/(2\pi)$. Labels A, I, P, and S on the top respectively indicate the auxiliary laser used for thermal compensation, the idler, the probe, and the soliton.

spectra are clean with no excess noise, indicating that we are indeed observing low-noise, stable frequency combs. Yet, each RF spectrum does exhibit a single sharp RF tone. This is because, whilst the idler comb inherits the line spacing of the soliton comb, the two are offset from one another [see Fig. 1(b)], resulting in beating between adjacent lines in the region where the combs overlap. The beat frequency $d\nu$ corresponds to the separation between the probe frequency and the soliton comb line closest to it. This can be written in terms of the soliton and probe detunings and the dispersive shift of the probe resonance as:

$$\frac{d\omega}{2\pi} = d\nu \approx \left[\delta_p - \delta_s + \frac{\beta_2 L \Omega_p^2}{2} \right] \text{FSR}. \quad (6)$$

In our experiments, the RF beat tones range from 30 to 140 MHz, and are hence far too small to be resolved optically. Indeed, the optical comb spectra shown in Fig. 3 were recorded at an optical spectrum analyzer (OSA) resolution of 5 GHz, and a careful examination of these traces reveals only a single set of equispaced comb lines. Likewise, further RF intensity-noise measurements made using an electronic spectrum analyzer reveal only a low-noise background out to a frequency of 10 GHz (in addition to the low-frequency RF beat-notes already observed in Fig. 3). Combined, these measurements confirm that the output spectrum is indeed composed of two individual low-noise combs: the first, the cavity soliton comb, and the second, the idler comb extending from the probe frequency to the phasematched idler peak, and spectrally offset from the cavity soliton.

The ability to measure the RF beat frequency between the soliton and the idler comb allows the two combs to be “stitched” together, i.e., the absolute frequencies of the idler comb lines to be directly related to the frequencies of the cavity soliton comb. In addition, when combined with measurements of the spectral position of the idler wave, the beat frequencies allow us to accurately estimate the parameters of the entire experiment (see Methods). Using parameters obtained in this manner (see caption of Fig. 2) in LLE simulations, we find excellent agreement with our experiments, as shown by the orange solid curves in Fig. 3(a)–(f). We observe particularly how the position and magnitude of the newly generated idler combs are very well reproduced by the simulations, and we also note that the idler positions are well predicted by the phasematched frequency given by Eq. (5).

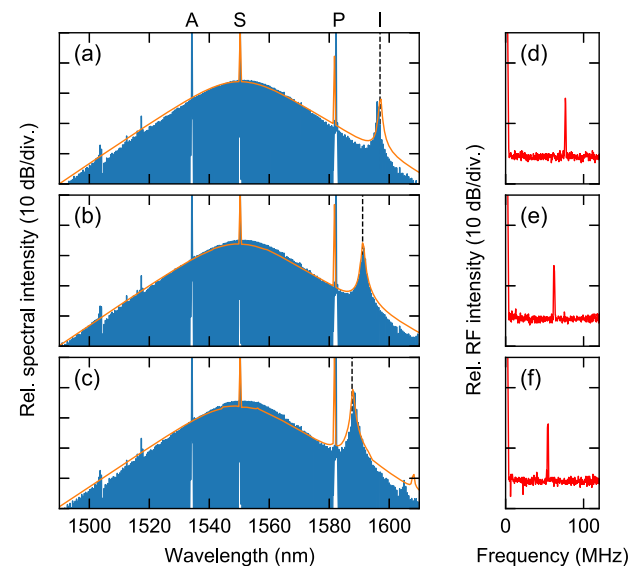


Fig. 4 Experimental spectra with positions of the soliton and probe waves interchanged. **a–c** The soliton is here generated at 1550 nm whilst the probe sits at 1582 nm. **d–f** Radio-frequency (RF) spectra corresponding to **(a–c)**. The results shown are for different negative values of the probe detuning. Orange curves show results from numerical simulations. Labels A, I, P, and S on the top respectively indicate the auxiliary laser used for thermal compensation, the idler, the probe, and the soliton.

The soliton and probe fields are interchangeable: we can exchange their roles by selecting appropriate detunings and still generate a phase-matched idler comb. To show this, we set the detuning of the 1550 nm laser such that it generates a cavity soliton, and use the 1582 nm laser as the external probe. Figure 4(a)–(c) show the output comb spectra as the probe field is continuously tuned into resonance from the blue-detuned (i.e., negative Δ_p) side, whilst Fig. 4(d)–(f) show the corresponding RF spectra. The observed spectra are qualitatively identical to those obtained when the 1582 nm pump generates the cavity soliton. Moreover, we again find excellent agreement between the experimentally recorded spectra and the numerical results obtained from the LLE (red traces). The only adjustment to the simulation parameters used in Figs. 2 and 3 was a change

to the value of the group-velocity dispersion coefficient $\beta_2 = -2.9 \times 10^{-27} \text{ s}^2 \text{ m}^{-1}$ due to the change in pump wavelength and residual third-order dispersion. The small spectral features visible in the experimentally measured spectra at ~ 1505 and 1515 nm are a result of mode crossings at these wavelengths⁴⁶. They play no significant role in the soliton-linear wave interaction and are not seen in our LLE simulations that consider only a single resonator mode family. Finally, we note in closing this section that for all the results presented here, the idler comb remains spectrally offset from the soliton comb ($\delta\nu \neq 0$). It is possible to envisage different experimental conditions where $\delta\nu$ could be set to zero. In this case, one would observe an interference between the contributions of the soliton and idler waves at each individual comb line. As the two lasers used to generate the soliton and probe driving fields are free-running independent lasers, this interference would be expected to vary on the timescale set by the two lasers' coherence times.

The results presented in Figs. 3 and 4 offer strong experimental support for the soliton-linear wave phasematching theory presented in the previous section. In addition to dynamics involving a single cavity soliton and the probe wave, our experiments show that more complex interactions can also take place. First, the soliton-linear wave interaction can occur when the resonator hosts several solitons. Indeed, in Fig. 5(a) we show comb spectra recorded at the resonator output with two temporally separated cavity solitons centred around a 1550 nm pump interacting with a probe field at 1582 nm; Fig. 5(b) shows the corresponding spectrum with the roles of the soliton-generating pump and the probe reversed. In both cases, a strong spectral modulation with a period of 4 nm can be observed, indicating the presence of two cavity solitons in the cavity separated by 2 ps. This spectral modulation manifests itself across both the cavity soliton and the idler combs, thus providing further evidence that the two combs are temporally locked to each other. Also shown in Fig. 5(a), (b) are theoretical sech^2 profiles of the cavity soliton spectral envelope in the absence of the probe wave. This shows how the soliton-linear wave interaction leads to a substantial increase in comb intensity around the probe. Finally, in accordance with the simulations shown in Fig. 2, our experiments show that a narrow region of probe detunings exist where the probe can undergo modulational instability whilst still allowing the cavity soliton and the idler comb to persist. Figure 5(c) shows the measured optical spectrum recorded in this regime, superimposed with corresponding simulations, and we indeed observe characteristic (i) modulation instability sidebands around the 1550 nm probe wavelength and (ii) soliton sech^2 profile around the 1582 nm cavity soliton pump. Moreover, the RF spectrum of this state [see Fig. 5(d)] shows clearly elevated level of intensity noise, as expected due to the chaotic nature of the modulation instability state.

Conclusion

To summarize, we have shown that the nonlinear interaction between a cavity soliton and an externally injected probe can engender spectral extension of a Kerr microcomb via the formation of a secondary idler comb. We have shown that the process is underpinned by a simple phasematching condition derived from the time-domain soliton-linear wave interaction picture, revealing that the probe field's linear detuning plays a key role in controlling the phasematched frequency – and hence the spectral characteristics of the idler comb. We obtain a simple linear phasematching expression for the frequency shift of the phasematched idler wave and find that, for our parameters, it agrees well with the numerical shifts predicted by a full LLE simulation. The idler and its generating soliton comb have the

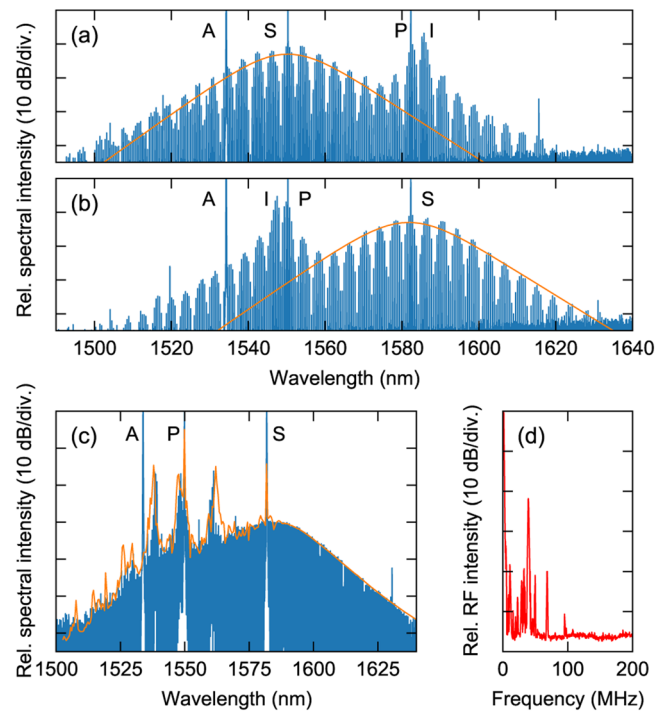


Fig. 5 Additional soliton-linear wave dynamics. Blue curves in (a), (b) show experimentally measured spectra at the resonator output when a two-cavity soliton state interacts with a probe. In (a) the solitons are at 1550 nm and the probe at 1583 nm, whilst in (b) the roles are swapped. The orange curves in (a), (b) show theoretically predicted cavity soliton envelopes in the absence of the probe wave, highlighting how the interaction leads to substantial spectral extension. c Blue and orange curves respectively show experimental and simulated optical spectra in the narrow parameter regime where the probe at 1550 nm undergoes modulation instability yet permits the cavity soliton at 1582 nm to persist. d shows the radio-frequency spectrum corresponding to (c), highlighting the low-coherence of the state. Labels A, I, P, and S respectively indicate the auxiliary laser used for thermal compensation, the idler, the probe, and the soliton.

same line spacing and low-noise characteristics, but are spectrally offset from one another; measurement of the RF beat frequency between the two combs allows the frequencies of the idler comb lines to be directly related to the cavity soliton comb. Combined, these properties make soliton-linear wave scattering an attractive candidate for the spectral expansion of Kerr combs, enabling comb power to be enhanced at desired spectral locations simply through the injection of an appropriate external probe field. We anticipate this ability could find useful application in many areas of microcomb research, including spectroscopy, frequency metrology and optical frequency synthesis. Finally, we close by emphasizing that the soliton-linear wave interaction described in our work represents the time-domain description of cascaded FWM Bragg scattering^{18,19}, which has been linked to microcomb spectral extension in recent works completed in parallel with our study¹⁷.

Methods

Experimental setup. Our setup is built around an MgF_2 micro-disk shaped via diamond point turning and then hand-polished to achieve a measured finesse of $\mathcal{F} \approx 3.1 \times 10^4$ at 1550 nm. The disk has a minor radius of $30 \mu\text{m}$, and a major radius of $600 \mu\text{m}$, yielding an free-spectral range of 58.4 GHz. A micron diameter fiber taper is used to couple the driving fields to and from the resonator. The microdisk is driven by three optical fields derived from two C-band external-cavity lasers (ECL), and one L-band ECL. Each laser is amplified by an erbium-doped-fiber amplifier, then filtered and coupled to the optical taper using fiber

wavelength-division-multiplexers. One of the C-band lasers and the L-band laser are coupled to the same mode family, and they can interchangeably act as the soliton-generating pump and the probe field. The remaining C-band laser (wavelength fixed at 1534 nm) is coupled to a different mode-family of the resonator and configured to act as an auxiliary pump that provides thermal compensation during the cavity soliton excitation. Throughout our measurements, the powers of the soliton and probe lasers were set to 80 mW whilst that of the auxiliary pump was set to 150 mW.

Bichromatically-pumped LLE Simulations. Our experimental observations are modelled by the Lugiato-Lefever equation (LLE)^{15,35–38}:

$$t_R \frac{\partial E(t, \tau)}{\partial t} = \left[-\alpha - i\delta_s - i\frac{\beta_2 L}{2} \frac{\partial^2}{\partial \tau^2} + i\gamma L |E|^2 \right] E + \sqrt{\theta} E_{\text{in}}(t, \tau). \quad (7)$$

Here $E(t, \tau)$ describes the slowly-varying intracavity electric field envelope, t is a “slow” time that describes the evolution of $E(t, \tau)$ at the scale of the photon lifetime, τ is a corresponding “fast” time that describes the envelope’s profile over a single roundtrip, $\alpha = \pi/\mathcal{F}$ is half of the power lost per round trip (and equal to the resonance half-width), δ_s is the phase detuning of the soliton-generating pump from the cavity resonance closest to it, and θ is the input power coupling coefficient. The driving field $E_{\text{in}}(t, \tau)$ accounts for the bi-chromatic pumping and is defined as

$$E_{\text{in}}(t, \tau) = E_{\text{in},s} + E_{\text{in},p} e^{-i\Omega_p \tau + i(\delta_p - \delta_s + \frac{\beta_2 L}{2} \Omega_p^2) \frac{\tau}{t_R}}, \quad (8)$$

where $E_{\text{in},s}$ and $E_{\text{in},p}$ are the pump amplitudes with units of $\text{W}^{1/2}$ at the soliton and probe frequencies ω_s and ω_p , respectively. All simulation results presented in the paper were obtained by numerically integrating Eq. (7) using the split-step Fourier method with parameters quoted in the caption of Fig. 2 (or elsewhere in the main text).

Fitting procedure. The following describes the procedure used to fit our simulations to our experimental data, allowing direct comparisons to be drawn. First, the change in probe detuning between each spectrum (shown in Fig. 2) can be calculated from the change in the measured RF beat notes, $\Delta d\nu$, as $\Delta\delta_p = 2\pi \cdot (\Delta d\nu / \text{FSR})$; second, the GVD coefficient β_2 can be extracted by fitting the change in idler position with the change in probe detuning: $\Delta\Omega_i = (\beta_2 L \Omega_i)^{-1} \Delta\delta_p$; third, γ and δ_s can be estimated by fitting numerical simulations to the cavity soliton spectrum, and to the measured value of δ_p at which the probe undergoes modulation instability. These procedures yield the parameters quoted in the caption of Fig. 2.

Data availability

The data that support the findings of this study are available from the corresponding author upon reasonable request.

Code availability

The code that supports the findings of this study are available from the corresponding author upon reasonable request.

Received: 31 December 2021; Accepted: 3 May 2022;

Published online: 24 May 2022

References

- Pasquazi, A. et al. Micro-combs generation of optical sources. *Phys. Rep.* **729**, 1–81 (2018).
- Kippenberg, T. J., Gaeta, A. L., Lipson, M. & Gorodetsky, M. L. Dissipative Kerr solitons in optical microresonators. *Science* **361**, eaan8083 (2018).
- Gaeta, A. L., Lipson, M. & Kippenberg, T. J. Photonic-chip-based frequency combs. *Nat. Photonics* **13**, 158–169 (2019).
- Pfeifle, J. et al. Coherent terabit communications with microresonator Kerr frequency combs. *Nat. Photonics* **8**, 375–380 (2014).
- Suh, M.-G., Yang, Q.-F., Yang, K. Y., Yi, X. & Vahala, K. J. Microresonator soliton dual-comb spectroscopy. *Science* **354**, 600–603 (2016).
- Trocha, P. et al. Ultrafast optical ranging using microresonator soliton frequency combs. *Science* **359**, 887–891 (2018).
- Suh, M.-G. & Vahala, K. J. Soliton microcomb range measurement. *Science* **359**, 884–887 (2018).
- Marchand, P. J. et al. Soliton microcomb based spectral domain optical coherence tomography. *Nat. Commun.* **12**, 427 (2021).
- Leo, F. et al. Temporal cavity solitons in one-dimensional Kerr media as bits in an all-optical buffer. *Nat. Photonics* **4**, 471–476 (2010).
- Herr, T. et al. Temporal solitons in optical microresonators. *Nat. Photonics* **8**, 145–152 (2014).
- Coen, S. & Erkintalo, M. Universal scaling laws of Kerr frequency combs. *Opt. Lett.* **38**, 1790–1792 (2013).
- Jang, J. K., Erkintalo, M., Murdoch, S. G. & Coen, S. Observation of dispersive wave emission by temporal cavity solitons. *Opt. Lett.* **39**, 5503–5506 (2014).
- Brasch, V. et al. Photonic chip-based optical frequency comb using soliton Cherenkov radiation. *Science* **351**, 357–360 (2016).
- Milián, C. & Skryabin, D. V. Soliton families and resonant radiation in a micro-ring resonator near zero group-velocity dispersion. *Opt. Exp.* **22**, 3732–3739 (2014).
- Zhang, S., Silver, J. M., Bi, T. & Del’Haye, P. Spectral extension and synchronization of microcombs in a single microresonator. *Nat. Commun.* **11**, 6384 (2020).
- Zhang, S. et al. Dark-Bright Soliton Bound States in a Microresonator. *Phys. Rev. Lett.* **128**, 033901 (2022).
- Moille, G. et al. Ultra-Broadband Kerr Microcomb Through Soliton Spectral Translation. *Nat. Commun.* **12**, 7275 (2021).
- Xu, Y. Q., Erkintalo, M., Genty, G. & Murdoch, S. G. Cascaded Bragg scattering in fiber optics. *Opt. Lett.* **38**, 142–144 (2013).
- Webb, K. E. et al. Nonlinear optics of fibre event horizons. *Nat. Commun.* **5**, 4969 (2014).
- Yulin, A. V., Skryabin, D. V. & Russell, S. J. Four-wave mixing of linear waves and solitons in fibers with higher-order dispersion. *Opt. Lett.* **29**, 2411–2413 (2004).
- Efimov, A. et al. Time-spectrally-resolved ultrafast nonlinear dynamics in small-core photonic crystal fibers: Experiment and modelling. *Opt. Exp.* **12**, 6498–6507 (2004).
- Skryabin, D. V. & Yulin, A. V. Theory of generation of new frequencies by mixing of solitons and dispersive waves in optical fibers. *Phys. Rev. E* **72**, 016619 (2005).
- Efimov, A. et al. Interaction of an Optical Soliton with a Dispersive Wave. *Phys. Rev. Lett.* **95**, 213902 (2005).
- Philbin, T. G. et al. Fiber-Optical Analog of the Event Horizon. *Science* **319**, 1367–1370 (2008).
- Demircan, A., Amirashvili, S. & Steinmeyer, G. Controlling Light by Light with an Optical Event Horizon. *Phys. Rev. Lett.* **106**, 163901 (2011).
- Bendahmane, A., Mussot, A., Conforti, M. & Kudlinski, A. Observation of the stepwise blue shift of a dispersive wave preceding its trapping by a soliton. *Opt. Exp.* **23**, 16595–16601 (2015).
- Ciret, C., Leo, F., Kuyken, B., Roelkens, G. & Gorza, S.-P. Observation of an optical event horizon in a silicon-on-insulator photonic wire waveguide. *Opt. Exp.* **24**, 114–124 (2016).
- Wai, P. K. A., Menyuk, C. R., Lee, Y. C. & Chen, H. H. Nonlinear pulse propagation in the neighborhood of the zero-dispersion wavelength of monomode optical fibers. *Opt. Lett.* **11**, 464–466 (1986).
- Akhmediev, N. & Karlsson, M. Cherenkov radiation emitted by solitons in optical fibers. *Phys. Rev. A* **51**, 2602–2607 (1995).
- Skryabin, D. V. & Gorbach, A. V. Colloquium: Looking at a soliton through the prism of optical supercontinuum. *Rev. Mod. Phys.* **82**, 1287–1299 (2010).
- Erkintalo, M., Dudley, J. M. & Genty, G. Pump-soliton nonlinear wave mixing in noise-driven fiber supercontinuum generation. *Opt. Lett.* **36**, 3870–3872 (2011).
- Erkintalo, M., Xu, Y. Q., Murdoch, S. G., Dudley, J. M. & Genty, G. Cascaded Phase Matching and Nonlinear Symmetry Breaking in Fiber Frequency Combs. *Phys. Rev. Lett.* **109**, 223904 (2012).
- Luo, K., Xu, Y., Erkintalo, M. & Murdoch, S. G. Resonant radiation in synchronously pumped passive Kerr cavities. *Opt. Lett.* **40**, 427–430 (2015).
- Skryabin, D. V. & Kartashov, Y. V. Self-locking of the frequency comb repetition rate in microring resonators with higher order dispersions. *Opt. Exp.* **25**, 27442–27451 (2017).
- Coen, S., Randle, H. G., Sylvestre, T. & Erkintalo, M. Modeling of octave-spanning Kerr frequency combs using a generalized mean-field Lugiato-Lefever model. *Opt. Lett.* **38**, 37–39 (2013).
- Chembo, Y. K. & Menyuk, C. R. Spatiotemporal Lugiato-Lefever formalism for Kerr-comb generation in whispering-gallery-mode resonators. *Phys. Rev. A* **87**, 053852 (2013).
- Hansson, T. & Wabnitz, S. Bichromatically pumped microresonator frequency combs. *Phys. Rev. A* **90**, 013811 (2014).
- Taheri, H., Matsko, A. B. & Maleki, L. Optical lattice trap for Kerr solitons. *Eur. Phys. J. D* **71**, 153 (2017).
- Anderson, M. et al. Coexistence of Multiple Nonlinear States in a Tristable Passive Kerr Resonator. *Phys. Rev. X* **7**, 031031 (2017).
- Nielsen, A. U., Garbin, B., Coen, S., Murdoch, S. G. & Erkintalo, M. Coexistence and Interactions between Nonlinear States with Different Polarizations in a Monochromatically Driven Passive Kerr Resonator. *Phys. Rev. Lett.* **123**, 013902 (2019).

41. Grudinin, I. S. et al. Ultra high Q crystalline microcavities. *Opt. Commun.* **265**, 33–38 (2006).
42. Strekalov, D. V., Marquardt, C., Matsko, A. B., Schwefel, H. G. L. & Leuchs, G. Nonlinear and quantum optics with whispering gallery resonators. *J. Opt.* **18**, 123002 (2016).
43. Sayson, N. L. B. et al. Octave-spanning tunable parametric oscillation in crystalline Kerr microresonators. *Nat. Photonics* **13**, 701–706 (2019).
44. Zhang, S. et al. Sub-milliwatt-level microresonator solitons with extended access range using an auxiliary laser. *Optica* **6**, 206–212 (2019).
45. Lu, Z. et al. Deterministic generation and switching of dissipative Kerr soliton in thermally controlled micro-resonator. *AIP Advances* **9**, 025314 (2019).
46. Herr, T. et al. Mode Spectrum and Temporal Soliton Formation in Optical Microresonators. *Phys. Rev. Lett.* **113**, 123901 (2014).

Acknowledgements

This work was supported by the Marsden Fund and the Rutherford Discovery Fellowships of the Royal Society of New Zealand.

Author contributions

P.C.Q. performed all the experiments. V.N. performed numerical modelling of resonators. F.A., L.S.T., and H.G.L.S. fabricated the resonators. M.E. and S.C. contributed to theoretical interpretation of the results. M.E. and S.G.M. wrote the manuscript. All authors contributed to discussing and interpreting the results.

Competing interests

The authors declare no competing interests.

Additional information

Supplementary information The online version contains supplementary material available at <https://doi.org/10.1038/s42005-022-00903-5>.

Correspondence and requests for materials should be addressed to Stuart G. Murdoch.

Peer review information *Communications Physics* thanks Dmitry Skryabin, Naoya Kuse and Xingyuan (Mike) Xu for their contribution to the peer review of this work. Peer reviewer reports are available.

Reprints and permission information is available at <http://www.nature.com/reprints>

Publisher's note Springer Nature remains neutral with regard to jurisdictional claims in published maps and institutional affiliations.



Open Access This article is licensed under a Creative Commons Attribution 4.0 International License, which permits use, sharing, adaptation, distribution and reproduction in any medium or format, as long as you give appropriate credit to the original author(s) and the source, provide a link to the Creative Commons license, and indicate if changes were made. The images or other third party material in this article are included in the article's Creative Commons license, unless indicated otherwise in a credit line to the material. If material is not included in the article's Creative Commons license and your intended use is not permitted by statutory regulation or exceeds the permitted use, you will need to obtain permission directly from the copyright holder. To view a copy of this license, visit <http://creativecommons.org/licenses/by/4.0/>.

© The Author(s) 2022